An Idealized Numerical Study of the Effects of Taiwan Topography on Typhoons

Ting-An Wang , Chun-Chieh Wu

Department of Atmospheric Sciences, National Taiwan University

and Yuh-Lang Lin

Department of Marine, Earth, and Atmospheric Sciences, North Carolina State University

1. Introduction

For a typhoon impinging on the Central Mountain Range (CMR) of Taiwan, Wang (1980, 1989) showed that the center of the storm can either cross Taiwan continuously or have a discontinuous track. The effects of CMR on typhoons include not only the track modification but also the structure adjustment. A recent observational study (Shieh et al., 1996) has categorized four flow regimes during typhoon invasions (Fig. 1): (a) the parallel flow regime, in which the flow field associated with typhoons basically moves along the CMR with a small incident flow angle (α in Fig. 1); (b) the blocked flow regime, where the incident angle is large enough and the Froude number (Fr) is low; (c) the unblocked (upsloping) flow regime, which is same as (b) but with a relatively high Fr; (d) the combined flow regime with low-level flow passing around but upper-level flow crossing over the mountain. The factors determining the above flow regimes include the typhoon's heading direction, the Froude number, the typhoon incident angle, and the location of the typhoon center.

The interaction between typhoons and the CMR is a complicated process, which has attracted a lot of research interests. In particular, several studies have been presented to discuss the effects of CMR on track modification. Chang (1982) showed that the mountain-induced flow deflections are mainly confined to the lower levels due to the blocking effects. Bender et al. (1987) suggested that the terrain-induced steering flow modification is the main cause of the typhoon track deflection, although there is large uncertainty on how to define the steering flow (Wu and Emanuel, 1995). Yeh and Elsberry (1993a,b) studied the upstream track deflections of westward-moving tropical cyclones approaching the mountainous terrain of Taiwan. They showed that the deflections tend to be larger for weaker and slower-moving storms. They also proposed a schematic summary of upstream track deflections in three regions for westward-moving tropical cyclones approaching Taiwan. Smith and Smith (1995) applied the shallow-water model to the problem of a typhoon drifting past Taiwan and demonstrated that many of the observed phenomena such as upstream blocking, downstream sheltering, corner winds, and foehn and secondary vortex formation can be captured. A real

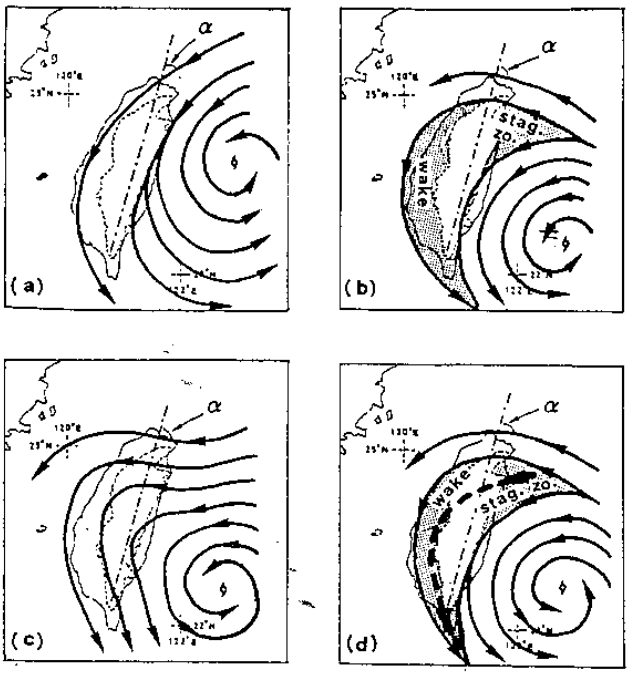

Fig. 1: Four flow regimes during typhoon invasions: (a) the parallel flow regime, (b) the blocked flow regime, (c) the unblocked (upsloping) flow regime, and (d) the combined flow regime. (After Shieh et al. 1996)

case simulation was presented by Wu and Cho (1996), where foehn and secondary vortex were also observed in their numerical results.

Mostly, tropical cyclones are considered to be driven by the steering flow. The steering concept is based on the assumption that tropical cyclones are isolated vorticity anomalies embedded in a background environment of larger-scale flow and thus move with the so-called "steering" flow. In this regard, the track modification can be understood through the investigation of how such a steering flow being modified by the CMR. However, before digging into the insight of such a challenging problem, it is important to have a clearer understanding on mountain flow dynamics.

During the past three decades, many efforts have been put on the study of the dynamics for a uniform flow past a mountain. Smith (1989a) proposed a linear theory to predict the occurrence of stagnation points as a function of hill shape and ambient shear. For a long

ridge perpendicular to a weakly sheared flow, stagnation begins aloft. Stagnation aloft is believed to cause gravity wave breaking and transition to a severe downslope wind configuration (Clark and Pieltier, 1977). For a ridge aligned with the flow, waves dispersively weaken aloft and stagnation occurs first on the surface. This allows density surfaces to intersect the ground and the low-level flow to split around the hill. As a ridge aligned more with flow, the critical mountain height for both the occurrence of stagnation upwind and aloft increase but the critical mountain height for stagnation aloft increases more rapidly. This is so because in three-dimensional flow the vertically propagating waves weaken aloft due to dispersion.

The salient features in the response of a density-stratified fluid flowing past a three-dimensional obstacle at low Fr are the existence of a flow reversal zone on the windward side and intense vertically oriented vortices on the lee side of the obstacle. The generation of lee vortices was explained as a consequence of the separation of the viscous boundary layer from the obstacle (Batchelor, 1967). However, Smolarkiewicz and Rotunno (1989, SR hereafter) argued that the lee vortices can be produced even in inviscid numerical simulations. They proposed that the mechanism for generation of the vertically oriented vorticity of the lee vortices is through the tilting of the horizontally oriented vorticity which is produced baroclinically as the isentropes deform in response to the flow over the obstacle. They believed that the lee vortices are closely associated with the dynamics of gravity waves and the conservation of potential vorticity (PV). However, Smith (1989b) argued that the conservation of PV is violated when stagnation points exist. Instead of considering the PV conservation, Smith (1989b) proposed a mechanism of PV generation to explain the formation of lee vortices.

In this study, the formation mechanisms for the occurrence of stagnation points for a three-dimensional flow over mountains will be investigated by a numerical model. The flow regimes, especially the critical Froude number for the occurrence of stagnation points, will be investigated through systematic numerical simulations. The flow regimes and the lee vortex formation mechanism will be then applied to explain the effects of the CMR on typhoons.

2. Numerical Model

The numerical model adopted in this study is the North Carolina State University Geophysical Fluid Dynamics Model (NCSU/GFDM), which is a three-dimensional hydrostatic primitive equation model in terrain-following coordinates, in which the Boussinesq and incompressible flow assumptions have been made. This model is designed to simulate flow over topography and/or diabatic forcing, to obtain a better understanding of the nonlinear dynamics in these types of problems.

The horizontal momentum equations, thermodynamic energy equation, incompressible continuity equation, and hydrostatic approximation to the vertical momentum equation governing thermally forced finite amplitude perturbations in a continuously stratified Boussinesq atmosphere may be written as:

$$\frac{\partial u'}{\partial t}+(U+u')\left[\frac{\partial u'}{\partial x}+G\frac{\partial u'}{\partial \sigma}\right]+(V+v')\left[\frac{\partial u'}{\partial y}+J\frac{\partial u'}{\partial \sigma}\right]+Hw'\frac{\partial}{\partial \sigma}(U+u')-fv'=-\left[\frac{\partial \pi'}{\partial x}+G\frac{\partial \pi'}{\partial \sigma}\right],$$

$$\frac{\partial v'}{\partial t}+(U+u')\left[\frac{\partial v'}{\partial x}+G\frac{\partial v'}{\partial \sigma}\right]+(V+v')\left[\frac{\partial v'}{\partial y}+J\frac{\partial v'}{\partial \sigma}\right]+Hw'\frac{\partial}{\partial \sigma}(V+v')+fu'=-\left[\frac{\partial \pi'}{\partial y}+J\frac{\partial \pi'}{\partial \sigma}\right],$$

$$\frac{\partial \theta'}{\partial t}+(U+u')\left[\frac{\partial \theta'}{\partial x}+G\frac{\partial \theta'}{\partial \sigma}\right]+\frac{f\theta_o u'H}{g}\frac{\partial V}{\partial \sigma}+(V+v')\left[\frac{\partial \theta'}{\partial y}+J\frac{\partial \theta'}{\partial \sigma}\right]-\frac{f\theta_o v'H}{g}\frac{\partial U}{\partial \sigma}+Hw'\frac{\partial}{\partial \sigma}(\Theta+\theta')=\frac{\overline{\theta}_o}{c_p\overline{T}_o}Q,$$

$$\left[\frac{\partial u'}{\partial x}+G\frac{\partial u'}{\partial \sigma}\right]+\left[\frac{\partial v'}{\partial y}+J\frac{\partial v'}{\partial \sigma}\right]+H\frac{\partial w'}{\partial \sigma}=0, \text{ and}$$

$$H\frac{\partial \pi'}{\partial \sigma}=g\frac{\theta'}{\theta_o}.$$

where
t = time,
x = horizontal coordinate in east-west direction,
y = horizontal coordinate in north-south direction,
σ = vertical coordinate,
U = basic horizontal wind velocity in x-direction,
V = basic horizontal wind velocity in y-direction,
u' = perturbation horizontal wind velocity in x-direction,
v' = perturbation horizontal wind velocity in y-direction,
w = perturbation vertical wind velocity in z coordinator,
θ' = perturbation potential temperature,
π' = perturbation kinematic pressure (p/ρ_o),
ρ_o = constant reference density,
T_o = constant reference temperature,
θ_o = constant reference potential temperature,
c_p = specific heat capacity of dry air at constant pressure,
Q = diabatic heating rate per unit mass ($J\ kg^{-1}\ s^{-1}$),
N = Brunt-Vaisala frequency,
f = Coriolis parameter, and
g = gravitational acceleration.

The Brunt-Vaisala frequency is assumed to be independent of height in this study. The relationship between σ and z is as follows:

$$\sigma=\frac{z_T[z-z_s(x,y)]}{z_T-z_s(x,y)}$$

G, J, H are defined as follows.

$$G\equiv\left.\frac{\partial \sigma}{\partial x}\right|_z=\frac{\sigma-z_T}{z_T-z_s}\frac{\partial z_s}{\partial x},$$

$$J\equiv\left.\frac{\partial \sigma}{\partial y}\right|_z=\frac{\sigma-z_T}{z_T-z_s}\frac{\partial z_s}{\partial y}, \text{ and}$$

$$H \equiv \frac{\partial \sigma}{\partial z} = \frac{z_T}{z_T - z_s},$$

where z_T is the top of the computational domain where $\sigma = z$, and $z_s(x,y)$ is the lower boundary.

For convenience in isolating the nonlinear effects, in this model the wind components in both x and y directions are separated into basic and perturbation parts, that is, (u, v) = (U+u', V+v'). The basic state wind fields are assumed to be functions of the vertical coordinate only. In other words, no horizontal shear of the basic flow is considered in this model.

The horizontal partial derivatives in the momentum, continuity, and thermo-dynamic energy equations are approximated using a fourth-order centered finite differencing scheme, while the vertical derivatives are approximated by a second-order centered finite differencing scheme. These schemes are similar to the numerical schemes employed in the Drexel Limited Area Mesoscale Prediction System (LAMPS) (Perkey, 1976), and are identical to the schemes employed in the two-dimensional z-coordinate version of the model employed by Lin et al. (1993). The Eulerian local accelerations or temporal derivatives appearing in the horizontal momentum and thermodynamic energy equations, which comprise the three prognostic equations of the numerical model, are approximated through the leapfrog scheme, with the exception of the first time step, which is computed by forward differencing.

As for the upper boundary condition, the model has the following three options: (1) Rigid lid, (2) Sponge layer (Klemp and Lilly, 1978) and (3) Radiation condition (Klemp and Durran, 1983), which allows energy to propagate out of the domain. Zero gradient or radiative lateral boundary conditions (Orlanski 1976) are employed. Five-point numerical smoothing (Shapiro, 1970) in space is employed in both the horizontal and vertical directions. Three-point numerical smoothing in time is also adopted (Asselin, 1972). The details of the numerical model can be found in Weglarz (1994) and in Lin and Wang (1996).

3. Numerical simulations

In this study, the Coriolis effects are excluded in the model and the flow is assumed to be inviscid. The bell-shaped topography is prescribed as

$$h(x,y) = h_o \Big/ \left\{ \left[(x - x_{mc})\cos\alpha - (y - y_{mc})\sin\alpha \right]^2 / a_x^{\,2} + \left[(x - x_{mc})\sin\alpha + (y - y_{mc})\cos\alpha \right]^2 / a_y^{\,2} \right\}^{1.5}$$

where h_o is the mountain height, α the orientation angle of the a_y-axis of the mountain range from north, (x_{mc}, y_{mc}) is the mountain center, and a_x and a_y the mountain half-widths in x and y directions, respectively.

a. The comparison with SR

Fig. 2 shows the comparison of the surface streamline pattern from the numerical model described in the previous section and that from SR for the cases with Fr=0.66 and 0.22. The solutions are shown after the nondimensional time $T=tU/a_x=9$ as in SR for direct comparison. The features of lateral deflection with Fr=0.66 and the lee vortices with Fr=0.22 found in SR are well reproduced in our simulations. There exists a flow reversal zone at the windward slope for the case with Fr=0.22. Smolarkiewicz et al. (1988) regarded the convergence associated with this zone to be primarily responsible for Hawaii's windward cloud band. In the upwind reversal zone, fluid parcels coming from near the ground upstream, upon reaching the obstacle, journey backward along the forward slope, and so, undercut oncoming parcels before exiting in the lateral direction. In the laboratory studies, the upwind flow reversal is explained by the adverse pressure gradient associated with the slowing of the wind upon reaching the obstacle and the lee vortices are due to the separation of the viscous boundary layer from the lower surface (Batchelor 1967). However, SR proposed that the lee vortices can be generated through inviscid process at low Fr due to the tilting of baroclinically produced horizontal vorticity.

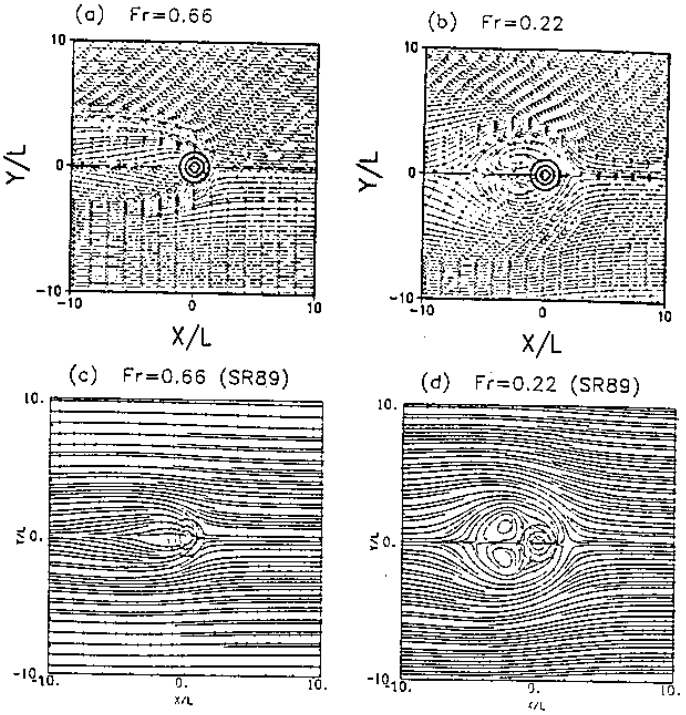

Fig. 2: Streamlines at the lower surface for Fr=0.66 and 0.22 from the numerical simulations of this study (a,b) and those from SRa (c,d).

Smith (1989a) proposed a regime diagram for the prediction of the critical Fr for the occurrence of stagnation aloft and at the upslope surface from linear solution. SR suggested that the stagnation point appears as Fr↘0.5, which is very close to the theoretical value of Fr≈0.4 proposed by Smith (1989a). However, when we integrate the case with Fr=0.66 for a longer time to T=40, the stagnation points at both windward and leeward surfaces are observed in the streamline field (not shown).

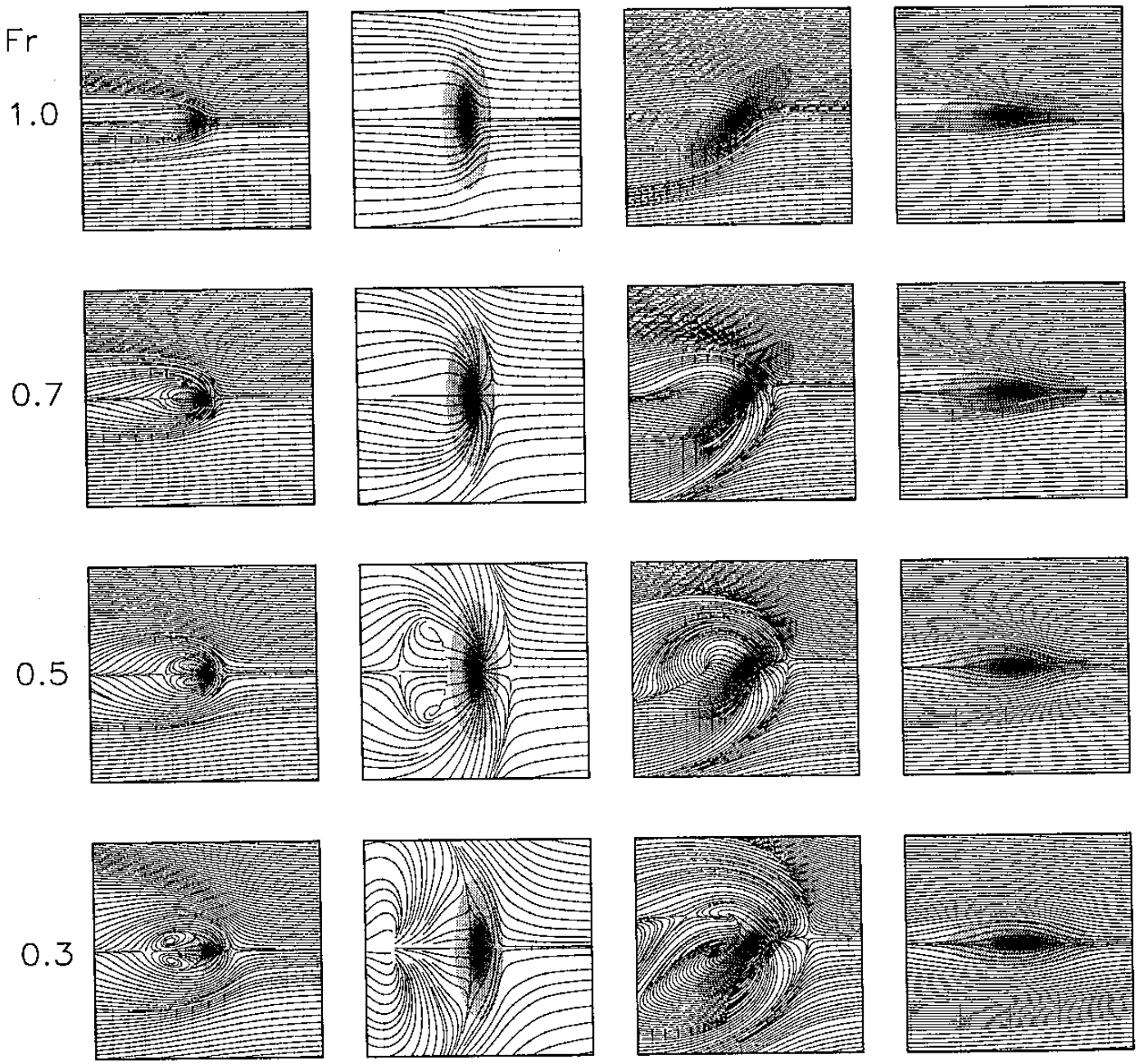

Fig. 3: Streamlines at the lower surface for flow passes a bell-shaped obstacle with aspect ratio $\beta=1$ and $\alpha=0°$ (the first column), $\beta=3$, $\alpha=0°$ (the second column), $\beta=3$, $\alpha=45°$ (the third column), and $\beta=1/3$, $\alpha=0°$ (the last column). The value of Fr is shown on the left of each row.

A similar result was also shown in Fig. 10 of Lin et al. (1992). Besides, the linear solution gives no suggestion of decelerated flow on the leeward side. Apparently, the prediction of the leeward stagnation point is beyond the reach of linear theory. A regime diagram for the critical Froude number for the windward and leeward stagnation point from nonlinear numerical simulations may be helpful for understanding the relationship between the upwind stagnation and leeward stagnation point and the flow dynamics behind.

b. Flow regimes with different β and α

Fig. 3 shows the surface streamline pattern for flow passes a bell-shaped obstacle with different aspect ratio β ($\equiv a_y/a_x$, i.e., across-stream half width/along-stream half width) and orientation angle α. Unless otherwise stated, the results will be shown after T=40. The first column in Fig. 3 shows the cases with β=1 and Fr=1.0, 0.7, 0.5, and 0.3 from the top to the bottom, respectively. Both the upwind reversal zone and lee vortices are observed in cases with Fr=0.7, 0.5, and 0.3, but not in that with Fr=1.0. It is obvious that the upstream reversal zone extends further upstream and the lee vortices become more organized as Fr decreases from 0.7 to 0.3. The second column in Fig. 3 shows the cases with β=3 and α=0°. For such an obstacle elongating in the direction normal to the mean flow, the upwind reversal zone extends more upstream and the extension of lee vortices is wider in y direction for the cases with Fr=0.3 and 0.5, as compared to those with β=1. However, the lee vortices are not observed in the case with Fr=0.7, although there exists a zone of reversed flow on the windward slope. *The above results suggest that the upwind stagnation is a necessary, but not a sufficient condition for the generation of lee vortices.* Besides, the blocking effects are enhanced while the lee deceleration is suppressed as the obstacle elongates in the direction normal to the mean flow. The streamlines for the cases with β=3 and α=45° are shown in the third column of Fig. 3. The upwind reversal zone is observed in the cases with Fr≤0.7 and the lee vortices are observed in those with Fr≤0.5. It is noted that the response is no more symmetric relative to x axis as those with α=0°. The area of the closed circulation on the lee side in the cases with Fr=0.5 and 0.3 is much larger to the left than to the right hand side, if one faces downstream. The last column shows the streamline of the cases with β=1/3 and α=0°. There exists neither upwind stagnation nor lee vortices even in the case with Fr=0.3. *Therefore, both the blocking effects and lee deceleration are depressed as the obstacle elongates in the direction along the mean flow.* Smolarkiewicz and Rotunno (1990) also found that the upwind stagnation disappears for small aspect ratio. This result is qualitatively in agreement with Smith's (1989a) flow-regime diagram, which predicts the disappearance of the lower upwind stagnation point as the obstacle elongates in the direction of the flow.

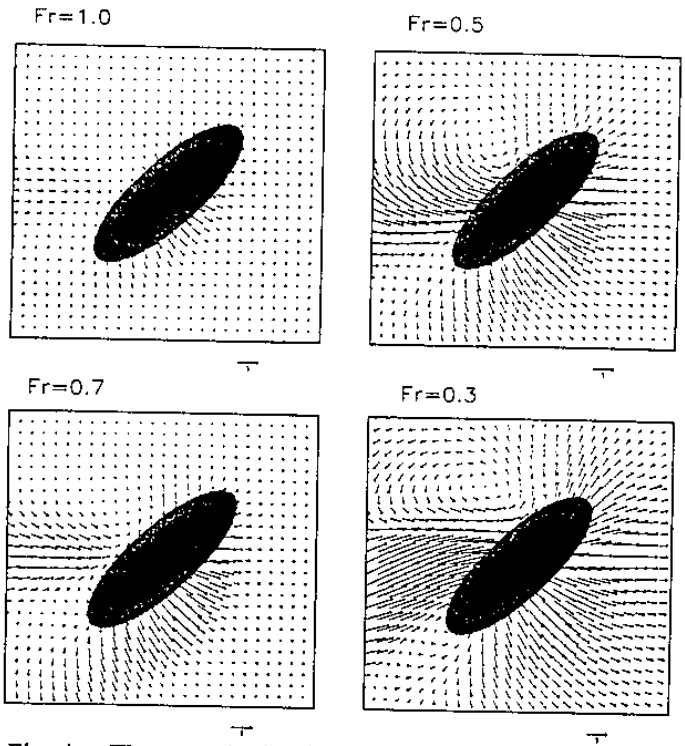

Fig. 4: The perturbation horizontal wind vector for the cases in the third column of Fig. 3.

Fig. 4 shows the dimensionless perturbation horizontal wind vector for the cases in the third column of Fig. 3, i.e., with β=3 and α=45°. The scale and orientation angle of the obstacle in these cases are designed to simulated the CMR. It is apparent that the strongest disturbance occurs at the third and fourth quadrant in each panel of Fig. 4. The flow response in this figure will be used as the control run when we discuss the simulations of the terrain effects on typhoons.

Fig. 5 shows the time evolution of the nondimensional zonal velocity (u) at surface along the y=0 axis. It is observed that a) upwind stagnation does not necessarily exist prior to the occurrence of lee reversal (e.g. Fig. 5d and 5l), b) the occurrence of upwind stagnation does not guarantee the existence of lee reversal (e.g. Fig. 5f and 5j), and c) the blocking effects are enhanced by the increase of β.

c. The role of nonlinearity

To help understand the exact role of nonlinearity in flow past a three-dimensional obstacle, we have also conducted a series of numerical simulations which exclude the nonlinear terms. Fig. 6 shows the comparison of nondimensional zonal velocity fields from nonlinear and linear numerical simulations for the cases with Fr=2.0, 1.0, and 0.5. Several features are observed in this figure. First, the disturbance is enhanced in both nonlinear and linear simulations as Fr decreases. Second, there exists no leeward reversal flow in linear simulation in the case with Fr=0.5, although the upwind reversal zone is observed. Third, it is apparent that the

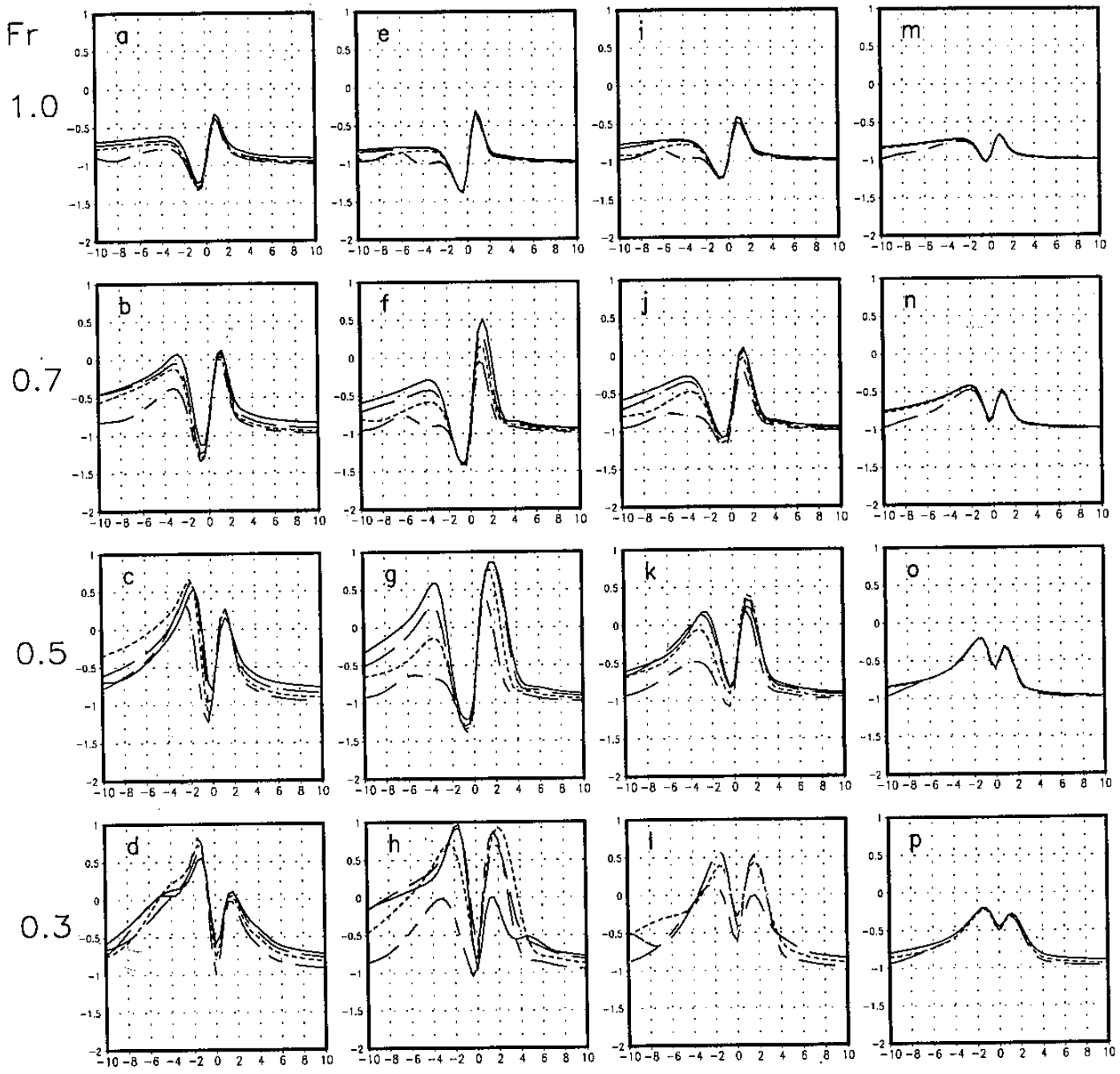

Fig. 5: Same as in Fig. 3 except for the time evolution of the nondimensional zonal velocity at y=0. Four times with T=10 , 20, 30, and 40 (solid lines) are plotted in each panel.

differences between the linear and nonlinear integrations increases as Fr decreases. The major difference between the linear and nonlinear results occurs on the lee side slope. *It is found that the major role of nonlinear terms is to decelerate the zonal flow on the central portion of lee surface. Therefore, the flow reversal zone at lee slope is primarily resulted from the nonlinear effects.* The distribution of nondimensional zonal velocity at y=0 (Fig. 7) clearly indicates that the linear results can well resolve the upstream response as compared to the nonlinear simulations. Meanwhile, as Fr decreases, the difference in magnitude is significantly enlarged.

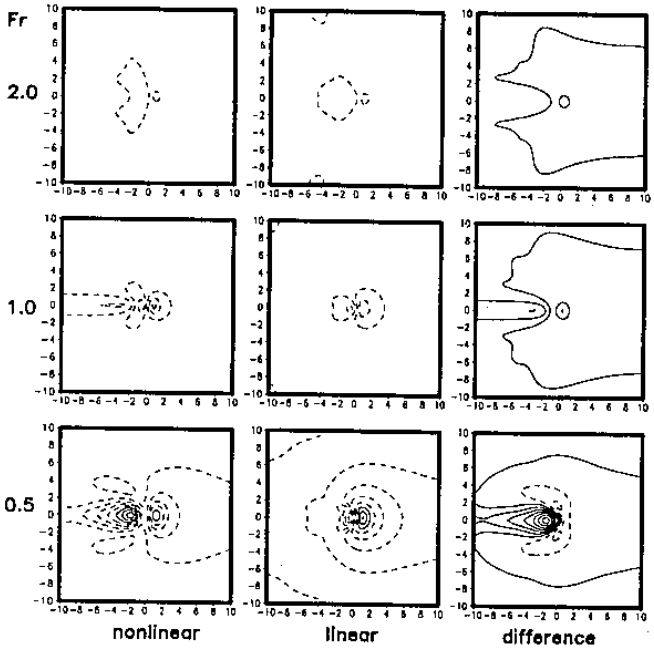

Fig. 6: The nondimensional zonal velocity fields at surface from nonlinear simulations (first column), linear simulations (second column), and the difference between the above two (third column) for the cases with Fr=2.0 (first row), 1.0 (second row), and 0.5 (third row).

Fig. 8 shows the x-σ vertical cross section of nondimensional zonal velocity fields from nonlinear (Fig. 8a) and linear (Fig. 8b) simulations for the case with Fr=0.5. *It is obvious that the vertically propagating gravity wave at higher level is much stronger in the linear simulations as compared to that in nonlinear ones.* The gravity wave propagates to a higher altitude in linear simulation, while it is suppressed in the nonlinear one. In the linear simulation for the case with Fr=0.22 (not shown), the wave overturning exists aloft in the vertical cross section, while no leeslope stagnation is observed. Wang and Lin (1996) indicate that wave overturning may occur in linear simulation, but the breaking wave cannot propagate downward due to the lack of nonlinear interaction.

Fig. 9 shows the vertically orientied vorticity at lower surface from nonlinear (Fig. 9a) and linear (Fig. 9b) simulations for the case with Fr=0.5. In Fig. 9a, there exists a positive (negative) vorticity on the right (left) hand side of the lee surface relative to downstream direction. A pair of positive and negative vorticity is also observed in linear simulations. However, the phase is opposite as compared to the nonlinear results.

It should be noted that this research is still in the preliminary stage at the moment writing this monograph.

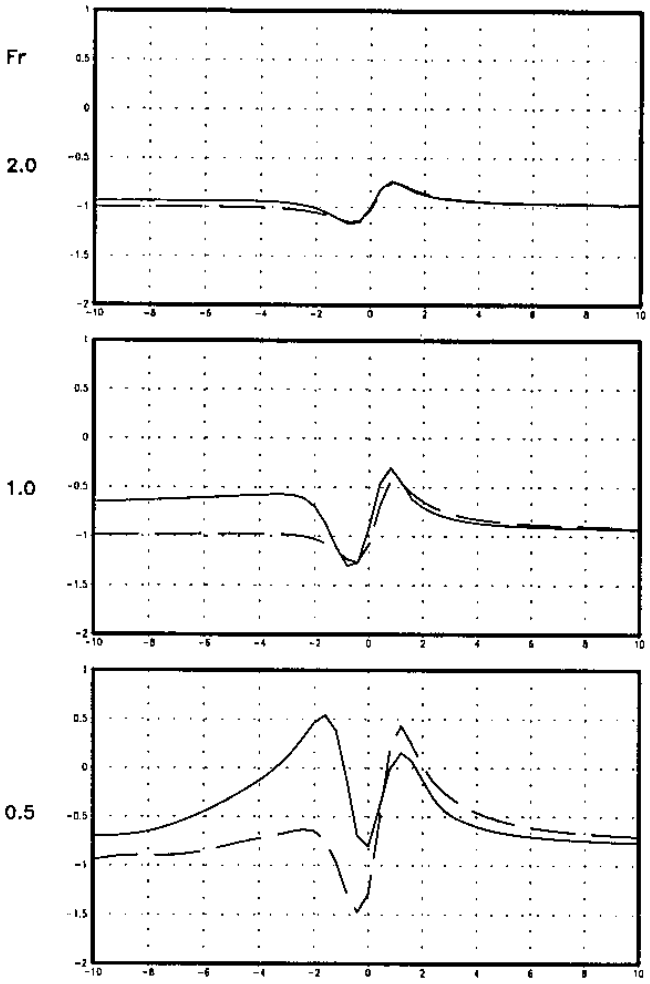

Fig. 7: The nondimensional zonal velocity at surface and y=0 of linear (dashed lines) and nonlinear (solid lines) simulations for the cases with (a) Fr=2.0, (b) Fr=1.0, and (c) Fr=0.5.

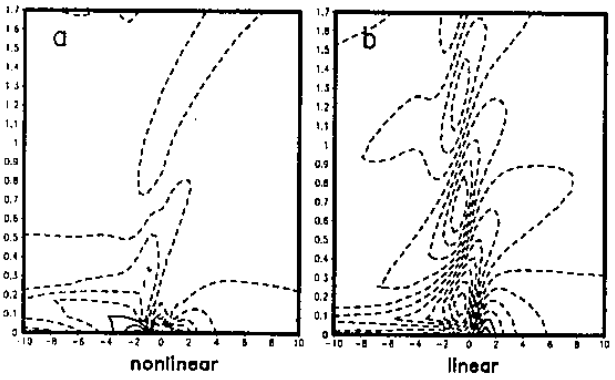

Fig. 8: The x-z vertical cross section of nondimensional zonal velocity at y=0 from (a) nonlinear and (b) linear simulations with Fr=0.5.

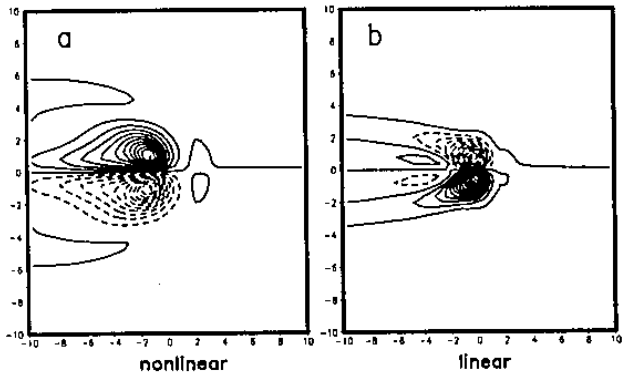

Fig. 9: The vertically oriented vorticity at surface from (a) nonlinear and (b) linear simulations with Fr=0.5.

To briefly summarized this work, it is found: *1) the upwind stagnation is a necessary rather than a sufficient condition for the generation of lee vortices; 2) both the upwind blocking effects and lee deceleration in the central portion are depressed as the obstacle elongates in the direction along the mean flow; 3) the major role of the nonlinear terms is to decelerate the zonal flow on the central portion of lee surface; 4) the vertically propagating gravity wave at higher levels is suppressed by the nonlinear terms.* The next step of this study will be to diagnose the sources of the vertically oriented vorticity on the lee side of the obstacle. The PV budget (Wu and Kurihara, 1996) will be analyzed to investigate the lee vortices formation mechanisms. The other objective of this study is to discuss the effects of terrain on typhoon. We will then initialized a vortex into the model to accomplish this task. It is hoped that a better understanding of the interaction between the CMR and typhoons can be provided through this research.

Acknowledgments

This work is supported by the grant NSC86-2811-M002-0034. The computations were performed on the DEC-alpha workstations at Department of Atmospheric Science of National Taiwan University.

References

Asselin, R. A., 1972: Frequency filter for time integration. Mon. Wea. Rev., **100**, 487-490.

Batchelor, G. K., 1967: An introduction to fluid dynamics. Cambridge University Press, 615 pp.

Bender, M. A., R. E. Tuleya, and Y. Kurihara, 1987: A numerical study of the effect of island terrain on tropical cyclones. Mon. Wea. Rev., **115**, 130-155.

Chang, S. W., 1982: The orographic effects induced by an island mountain range on propagating tropical cyclones. Mon. Wea. Rev., **110**, 1255-1270.

Clark, T. L., and W. R. Peltier, 1977: On the evolution and stability of finite-amplitude mountain waves. J. Atmos. Sci., **34**, 1715-1730.

Klemp, J. B., and D. R. Durran, 1983: An upper boundary condition permitting internal gravity wave radiation in numerical mesoscale models. Mon. Wea. Rev., **111**, 430-444.

Klemp, J. B., and D. K. Lilly, 1978: Numerical simulation of hydrostatic mountain waves. J. Atmos. Sci., **32**, 78-107.

Lin, Y.-L., 1993: Orographic effects on airflow and mesoscale weather systems over Taiwan. TAO, **4**, 381-420.

Lin, Y.-L., N.-H. Lin, and R. P. Weglarz, 1992: Numerical modeling studies of lee mesolows, mesovortices and mesocyclones with application to the formation of Taiwan mesolows. Meteor. Atmos. Phys., **49**, 43-67.

Lin, Y.-L., D. W. Hamilton, and C.-Y. Huang, 1996: Orographic influence on propagating cyclones. Mon. Wea. Rev., in press.

Lin, Y.-L., and T.-A. Wang, 1996: Flow regimes and transient dynamics of two-dimensional stratified flow over an isolated mountain ridge. J. Atmos. Sci., **53**, 139-158.

Lin, Y.-L., T.-A. Wang, and R. P. Weglarz, 1993: Interactions between gravity waves and cold air outflows in a stably stratified uniform flow. J. Atmos. Sci., **50**, 3790-3816.

Orlanski, I., 1976: A simple boundary condition for unbounded hyperbolic flow. J. Comput. Phys., **21**, 251-269.

Perkey, D. J., 1976: A description and preliminary results from a fine mesh model for forecasting quantitative precipitation. Mon. Wea. Rev., **104**, 1513-1526.

Shapiro, R., 1970: Smoothing, filtering, and boundary effects, Rev. Geophys., **8**, 359-387.

Shieh, S.-L, S.-T. Wang, M.-D. Cheng, and T.-C. Yeh, 1996: User's guide for typhoon forecasting in the Taiwan area. Res. Rep. CWB83-1M-01, 356 pp.

Smith, R. B., 1989a: Mountain-induced stagnation points in hydrostatic flow. Tellus, **41A**, 270-274.

Smith, R. B., 1989b: Comment on "Low-Froude-number flow past three-dimensional obstacles. Part I: Baroclinically generated lee vortices." J. Atmos. Sci., **46**, 3611-3613.

Smith, R. B., and D. F. Smith, 1995: Pseudoinviscid wake formation by mountains in shallow-water flow with a drifting vortex. J. Atmos. Sci., **52**, 436-454.

Smolarkiewicz, P., R. Rasmussen and T. L. Clark, 1988: On the dynamics of Hawaiian cloud bands: Island forcing. J. Atmos. Sci., **45**, 1872-1905.

Smolarkiewicz, P., and R. Rotunno, 1989 (SR): Low-Froude number flow past three dimensional obstacles. Part I: Baroclinically generated lee vorticies. J. Atmos. Sci., **46**, 1154-1164.

Smolarkiewicz, P., and R. Rotunno, 1990: Low-Froude number flow past three dimensional obstacles. Part II: Upwind flow reversal zone. J. Atmos. Sci., **47**, 1498-1511.

Wang, S.-T., 1980: Prediction of the behavior and strength of typhoons in Taiwan and its vicinity. Res. Rep. 108, National Science Council, Taipei, Taiwan, 100 pp.

Wang, S.-T., 1989: Observational analysis of the orographically induced disturbances during TAMEX. Workshop on TAMEX Preliminary Scientific Results, 279-286, Taipei, Taiwan.

Wang, T.-A. and Y.-L. Lin, 1996: Effects of critical level in a stratified shear flow. Part II: On mechanisms of severe downslope windstorm. Submitted to J. Atmos. Sci. for publication.

Weglarz, R. P., 1994: Three-dimensional geostrophic adjustment of rotating homogeneous and continuously stratified atmospheres with application to the dynamics of midlatitude jet streaks, Ph.D. thesis, 414 pp., North Carolina State Univ., Raleigh.

Wu, C.-C., and Y.-T. Cho, 1996: The observational analysis and numerical simulations of the effects of Taiwan topography on typhoon Gladys (1994). The Fifth Conference on Atmospheric Sciences, 26-29 June, Taipei, Taiwan, 340-349.

Wu, C.-C., and K. A. Emanuel, 1995: Potential vorticity diagnostics of hurricane movement. Part I: A case study of hurricane Bob (1991). Mon. Wea. Rev., **123**, 69-92.

Wu, C.-C., and Y. Kurihara, 1996: A numerical study of the feedback mechanisms of hurricane-environment interaction on hurricane movement from the potential vorticity perspective. J. Atmos. Sci., **53**, 1398-1416.

Yeh, T.-C., and R. L. Elsberry, 1993a: Interaction of typhoons with the Taiwan orography. Part I. Upstream track deflections. Mon. Wea. Rev., **121**, 3193-3212.

Yeh, T.-C., and R. L. Elsberry, 1993b: Interaction of typhoons with the Taiwan orography. Part II. Continuous and discontinuous tracks across the island. Mon. Wea. Rev., **121**, 3213-3233.